International Journal of
Molecular Sciences

MDPI

Article

Effect of Ni Substitution on the Structural, Magnetic, and Electronic Structure Properties of $Gd_{0.4}Tb_{0.6}(Co_{1-x}Ni_x)_2$ Compounds

Marcin Sikora [1], Anna Bajorek [1], Artur Chrobak [1], Józef Deniszczyk [2], Grzegorz Ziółkowski [1] and Grażyna Chełkowska [1,*]

[1] Institute of Physics, University of Silesia in Katowice, 41-500 Chorzów, Poland
[2] Institute of Materials Engineering, University of Silesia in Katowice, 41-500 Chorzów, Poland
* Correspondence: grazyna.chelkowska@us.edu.pl

Abstract: The comprehensive research of magnetic and electronic structure properties of the new class of $Gd_{0.4}Tb_{0.6}(Co_{1-x}Ni_x)_2$ compounds, crystallizing in the cubic Laves phase (C15), is reported. The magnetic study was completed with electrical resistivity and electronic structure investigations. The analysis of Arrott plots supplemented by a study of temperature dependency of Landau coefficients revealed that all compounds undergo a magnetic phase transition of the second type. Based on magnetic isotherms, magnetic entropy change (ΔS_M) was determined for many values of the magnetic field change ($\mu_0 H$), which varied from 0.1 to 7 T. For each compound, the ΔS_M had a maximum around the Curie temperature. Both values of the $|\Delta S_M{}^{max}|$ and relative cooling power *RCP* parameters increased with increasing nickel content. It is shown that structural disorder upon Co/Ni substitution influences some magnetic parameters. The magnetic moment values of Co atoms determined from different methods are quantitatively consistent. From the $M(T)$ dependency, the exchange integrals J_{RR}, J_{RT}, and J_{TT} between rare-earths (R) and transition metal (T) moments were evaluated within the mean-field theory (MFT) approach. The experimental study of the electronic structure performed with the use of the X-ray photoelectron spectroscopy (XPS) was completed by calculations using the full-potential linearized augmented plane waves (FP-LAPW) method based on the density functional theory (DFT). The calculations explained experimentally observed changes in the XPS valence band spectra upon the Ni/Co substitution.

Keywords: magnetic properties; rare earth–transition metal compounds; magnetocaloric effect; electrical resistivity; electronic structure

Citation: Sikora, M.; Bajorek, A.; Chrobak, A.; Deniszczyk, J.; Ziółkowski, G.; Chełkowska, G. Effect of Ni Substitution on the Structural, Magnetic, and Electronic Structure Properties of $Gd_{0.4}Tb_{0.6}(Co_{1-x}Ni_x)_2$ Compounds. *Int. J. Mol. Sci.* **2022**, *23*, 13182. https://doi.org/10.3390/ijms232113182

Academic Editor: Vasile Chiş

Received: 6 October 2022
Accepted: 25 October 2022
Published: 29 October 2022

1. Introduction

Among magnetic materials, RCo_2 compounds (R = rare earth) having the Laves phase structure of C15 type have attracted particular interest [1,2]. Attention to these materials is mainly due to their attractive properties, which strongly depends on the type of rare-earth element in the composition [3]. Furthermore, their simple cubic crystal structure facilitates the interpretation of the obtained results. The RCo_2 compounds with nonmagnetic R-ions, such as Y or Lu, show enhanced Pauli paramagnetism and underwent a metamagnetic transition [1,3]. Under the influence of an external magnetic field exceeding a certain critical H_c value, a transition from a paramagnetic to a ferromagnetic state occurs accompanied by the increase in initially negligible magnetic moments on the Co site, even by 0.5 μ_B [4,5]. In RCo_2 compounds with magnetic R-ions, cobalt atoms have induced magnetic moment, which occurs due to the 4*f*-3*d* interaction between localized moments of rare earth and the metamagnetic moments of cobalt [1]. Substitution of other kinds of atoms in RCo_2 results in a new family of compounds called pseudobinaries, such as the $R(Co_{1-x}T_x)_2$, the $R_{1-y}R'_yCo_2$, or even four-component $R_{1-y}R'_y(Co_{1-x}T_x)_2$ compounds (R′—rare earth, T—3*d* element). They are particularly interesting because of additional interactions between

magnetic moments (4f'-4f, 4f-3d, 4f'-3d, and others), which may significantly alter the magnetic properties of the original material but also strongly modify their electronic structure. It is known that RCo_2 compounds show a magnetic structure with parallel or antiparallel alignments of the magnetic moments of R and Co ions for light or heavy R elements, respectively [2]. RCo_2 compounds are also known as materials exhibiting a significant magnetocaloric effect (MCE) [1].

Magnetic cooling based on the magnetocaloric effect is considered an alternative cooling technique to classical gas vapor cooling due to its high efficiency and environmental friendliness. The value of MCE in these compounds usually has its maximum around the Curie temperature (T_C) and can be pretty high in the case of the first-order phase transition (FOPT). The magnetic materials for which T_C is located near room temperature are particularly attractive due to the possibility of using them for magnetic refrigeration in consumer devices. Recently, we reported on the comprehensive experimental and theoretical studies of magnetic and electronic structural properties of the $Gd_{0.4}Tb_{0.6}Co_2$ compound [6], for which the T_C was earlier determined to be near room temperature [7]. We have shown that this compound is a material with minimal hysteresis losses and reasonable relative cooling power (RCP) parameter values at room temperature, which qualifies it for use in magnetic refrigerators. Considering the $Gd_{0.4}Tb_{0.6}Co_2$ as a basis for the new class of four-component compounds, we have studied the $Gd_{0.4}Tb_{0.6}(Co_{1-x}Ni_x)_2$ system. We investigated its electronic structure, particularly in the valence band range, essential for magnetic properties. The study of the electronic structure was conducted experimentally and theoretically. Our results are entirely new for the system under investigation. Moreover, using the two-sublattice model, in the mean-field theory (MFT) approximation, the exchange integrals J_{RR}, J_{RCo}, and J_{CoCo} were evaluated. Within this theory, we determined the magnetic moment of Co atom, $\mu_{Co\text{-}MFT}$, and compared it with its values obtained by other methods.

2. Results and Discussion

2.1. Crystal Structure

The crystal structure of all analyzed compounds was refined using the Rietveld method, and the analysis was carried out using noncommercial Maud software ver. 1.6.4 (Pandata, Berlin, Germany) [8,9]. The study showed that the samples with x = 0.00, 0.05, 0.10, 0.15, and 0.50 crystallized in the $MgCu_2$ type of structure (Fd-3m space group) and were free from undesirable magnetic impurities. In contrast, the sample with x = 0.80 contained additionally about 3.5% of the $Gd_{40}Tb_{60}$ phase. The sample with x = 1.00 crystallized in the superstructure of $MgCu_2$ with double cell parameter a and contained two additional undesirable magnetic phases (Tb_2O_3, 9.8%) and TbNi (7.2%). With increasing Ni content, the value of the a, which for the $Gd_{0.4}Tb_{0.6}Co_2$ compound was equal to 7.256 Å $\pm$ 0.001 Å, first decreases rapidly for x less than 0.15 and then for higher concentrations decreases following Vegard's law (Figure 1, left axis). The cell parameter generally lowers because nickel atoms have smaller ionic radii than cobalt atoms. The deviation from Vegard's law, visible for small Ni concentration (<0.15) can be attributed to magneto-volume effects, as the measurements (at 294 K) have been carried out not far away from T_C. A similar situation was observed in $Gd(Co_{1-x}Ni_x)_2$ compounds [10,11].

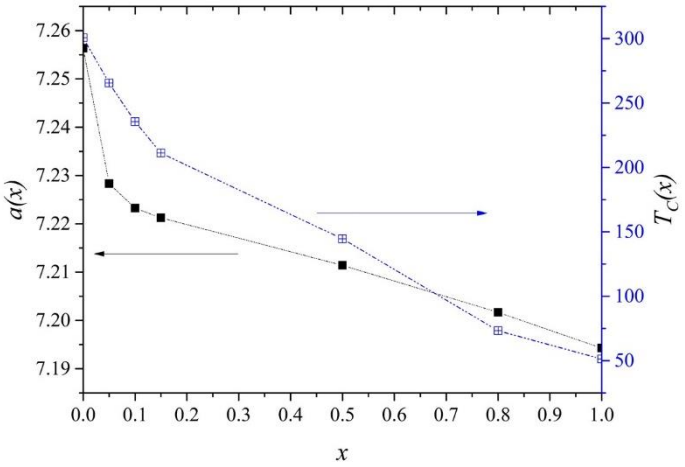

Figure 1. Lattice parameter a as a function of x (left axis). Curie temperature T_C derived from magnetic measurements, discussed in Section 2.2 (right axis).

2.2. Magnetic Properties

The temperature dependence of the magnetization $M(T)$ measured in zero-field cooling (ZFC) and field cooling (FC) mode at the external magnetic field of 0.1 T is shown in Figure 2.

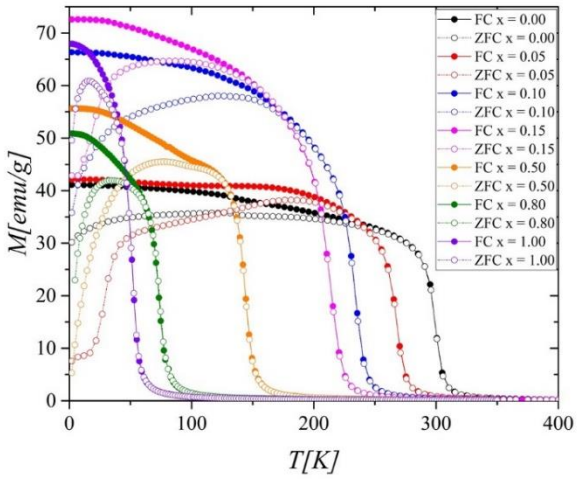

Figure 2. Magnetization M versus temperature, measured in FC and ZFC mode (M_{FC} and M_{ZFC}) at a magnetic field of 0.1 T.

The thermomagnetic curves exhibit irreversible behavior in the low-temperature range. The difference between the M_{FC} and M_{ZFC} at 2 K changes with Ni concentration and is most significant for $x = 0.5$ (Figure 3).

Several reasons may be responsible for the observed M_{FC}-$M_{ZFC}(x)$ differences. Some of these include structural and magnetic disorders; others point to spin–orbit coupling changes that influence magnetic anisotropy, the domain wall pinning effect, or the impact of the crystal field [12–17]. According to our results discussed later, we are rather convinced that the indicated difference is due to structural and magnetic disorders.

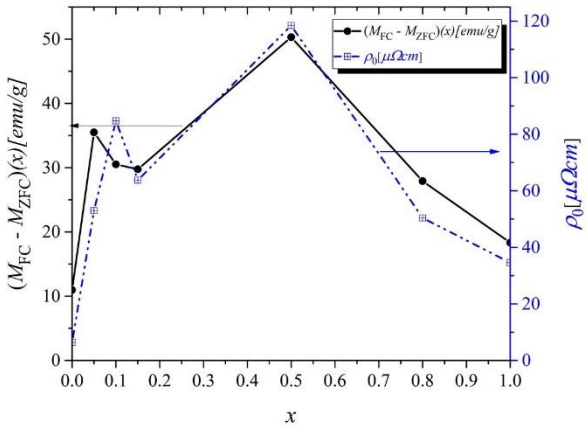

Figure 3. Difference between the M_{FC} and M_{ZFC} values at 2 K (left axis). Residual resistivity (ρ_0) vs. concentration x, discussed in Section 2.4 (right axis).

The real parts of the magnetic susceptibility *AC* ($\chi'(T)$ in Figure 4) showed characteristic peaks at magnetic transition temperatures T_C. The values of T_C determined from χ' 1 and from minima of dM/dT in both ZFC and FC modes are in perfect agreement, showing a significant decrease with increasing Ni content (Figure 1, right axis). This effect can be related to the dilution of the Co subsystem when replacing Co atoms with weaker magnetically Ni atoms. Similar behavior was observed in many Laves phase compounds doped by nickel [18,19]. The noticeable consistency of $a(x)$ and $T_C(x)$ plots confirm that T_C and magnetic properties have a strong lattice volume dependence in these compounds [10,20].

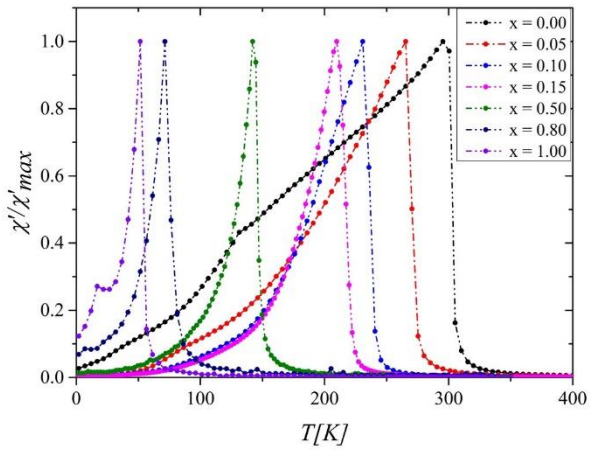

Figure 4. The real part of the *AC* magnetic susceptibility χ' normalized against the maximum value of χ'_{max} for the $Gd_{0.4}Tb_{0.6}(Co_{1-x}Ni_x)_2$.

The hysteresis loops measured at 2 K, 25 K, 50 K, 100 K, and 300 K show minimal hysteresis losses for all investigated samples (Figure 5). Moreover, no saturation has been observed even at $\mu_0 H = 7$ T. Using $M(H)$ data at 2 K, the saturation magnetization (M_S) was determined from extrapolation to zero of $1/H$ in the M vs. $1/H$ dependence. The value of M_S grew monotonically with the nickel content, except for the sample with $x = 1.0$ (Table 1). Using the obtained values for M_S, we estimated the magnetic moment of the 3*d* sublattice ($2\ \mu_{3d}$) versus x, applying the formula $M_S = 0.4\ \mu_{Gd} + 0.6\ \mu_{Tb} + 2\ \mu_{3d}$ with $\mu_{3d} = (1 - x)\ \mu_{Co} + x\ \mu_{Ni}$, $\mu_{Gd} = 7\ \mu_B$, and $\mu_{Tb} = 9\ \mu_B$. For $x = 0$ ($M_S = 5.86\ \mu_B$), the procedure gave $\mu_{Co} = -1.17\ \mu_B$, which is in accordance with earlier results in these kinds of compounds [6,11]. The negative sign indicates the antiparallel alignment of the R and Co moments. With the growing content of Ni, which is nearly nonmagnetic [11,21], the 3*d* sublattice moment $2\ \mu_{3d}$ decreases (Table 1). Because μ_{3d} and μ_R are oriented antiparallel, it yields the observed increase in $M_S(x)$.

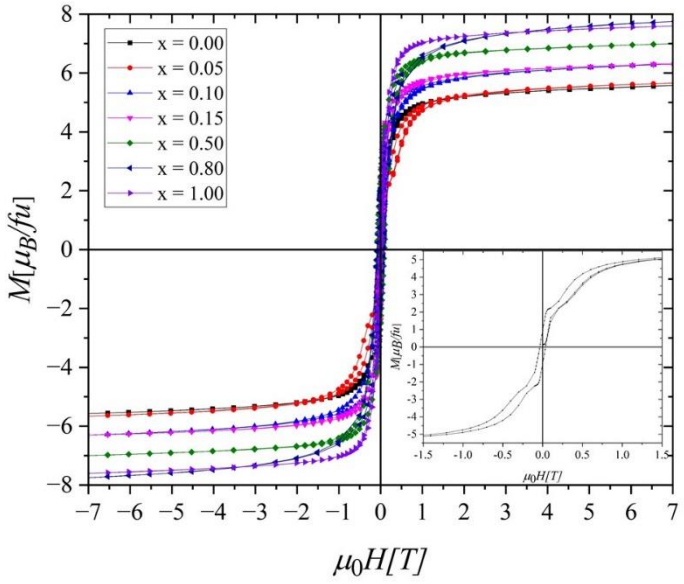

Figure 5. Hysteresis loops measured at 2 K. The inset shows $M(\mu_0 H)$ in the low magnetic field values range for the sample with x = 0.05.

Table 1. Curie temperature (T_C), saturation magnetization (M_S), and 3*d* sublattice contribution to the magnetic moment (2 μ_{3d}) in the $Gd_{04}Tb_{0.6}(Co_{1-x}Ni_x)_2$ system. In the table, the *exp.* and the *calc.* denote the experimental and ab initio results. The results denoted as *fit* were estimated using the formula $M_S(x)$ = 2.104 x +5.942 obtained by fitting the linear function to ab initio results for M_S (R square = 0.998).

x		0.00	0.05	0.10	0.125	0.15	0.25	0.375	0.50	0.80	1.00
T_C [K]		300.6	265.4	235.6	-	215.6	-	-	144.5	73.3	51.3
M_S [μ_B/fu]	*exp.*	5.86	5.94	6.57	-	6.60	-	-	7.20	8.10	7.83
	calc.	5.91			6.17		6.51	6.78	7.02		8.07
	fit	5.94	6.05	6.15	6.21	6.26	6.47	6.73	7.2	7.62	8.05
2 μ_{3d} [μ_B/fu]	*exp.*	2.34	2.26	1.63	-	1.60	-	-	1.00	0.10	0.37
	calc.	2.57	-	-	2.26	-	1.93	1.64	1.39	-	0.24

All the hysteresis loops show a symmetric course after changing the external magnetic field direction; however, for the sample with x = 0.05, a slight deformation was observed in the $M(H)$ chart, suggesting a coexistence of hard and soft magnetic phases (inset of Figure 5). Materials showing such behavior are known as exchange spring magnets [22,23]. In the case of our sample, it may be related to the presence of a foreign magnetic phase in tiny amounts below the XRD detectability.

Figure 6a,b shows the residual magnetization M_R and coercive fields H_c as a function of T in the $Gd_{0.4}Tb_{0.6}(Co_{1-x}Ni_x)_2$ system. As can be seen, with the increase in the nickel content, the H_c measured at 2 K grows up to the maximum value of 0.083 T for x = 0.5, then decreases to 0.005 T for x = 0.8 (inset in Figure 6b). A similar trend, with a maximum at the same Ni concentration, was observed for $M_R(x)$ (inset in Figure 6a). A slight rise of the H_c value for x = 1.0 might be related to additional magnetic phases in the sample. The $H_c(x)$ dependence perfectly reflects the $\rho_0(x)$ dependence (which will be discussed later) and is consistent with the M_{FC}-M_{ZFC} one (Figure 2). Thus, all these dependencies appear to have a common origin: the structural disorder and magnetocrystalline anisotropy influence that occur with doping.

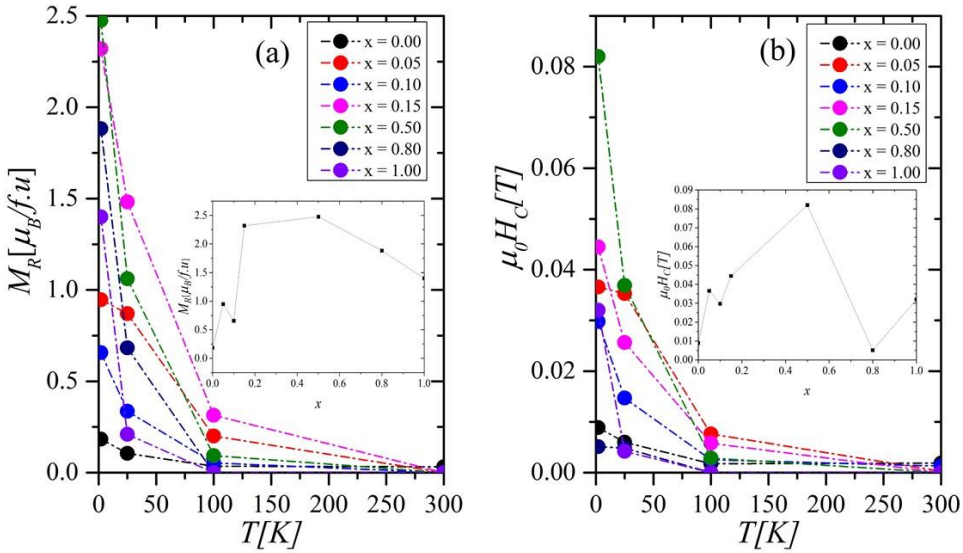

Figure 6. The residual magnetization M_R (**a**) and coercive fields H_C (**b**) versus T and chemical composition x in the $Gd_{04}Tb_{0.6}(Co_{1x}Ni_x)_2$ compounds. The insets in Figure (**a**) and (**b**) present the concentration dependence of M_R and H_c, respectively.

The magnetic properties of materials containing R (4*f*) and T (3*d*) elements are determined by exchange interactions between spins of constituent atoms. The strength of these interactions is described by the exchange integrals J_{RR}, J_{TT}, and J_{RT} (= J_{TR}). To estimate the 3*d*-3*d* and 3*d*-4*f* exchange interactions in $Gd_{0.4}Tb_{0.6}(Co_{1-x}Ni_x)_2$ compounds, we considered its magnetic structure as consisting of two magnetic sublattices formed by R(Gd/Tb) and T(Co/Ni) moments. We performed the estimation by applying the approach described in detail in [6,24,25]. In the evaluation, we used the $M(T)$ dependence under the magnetic field of 5 T, which was high enough to avoid the influence of domain effects and achieve a relatively high saturation (black curves in Figure 7). Table 2 shows the results of exchange coupling integrals calculated under the assumption that the average coordination numbers of RR (Z_{RR}), RT (Z_{RT}), TR (Z_{TR}), and TT (T_{TT}) are equal: 4, 12, 6, and 6, respectively [26].

Table 2. The exchange integrals J_{RR}, J_{RT}, J_{TT}, and magnetic moments of the 3*d* sublattice calculated in the framework of MFT theory (2 $\mu_{3d\text{-}MFT}$).

$Gd_{0.4}Tb_{0.6}(Co_{1-x}Ni_x)_2$	J_{RR} [10^{-23}J]	$-J_{RT}$ [10^{-23}J]	J_{TT} [10^{-22}J]	2 $\mu_{3d\text{-}MFT}$ [μ_B/fu]
x = 0.00	1.90	11.7	3.59	2.44
x = 0.05	1.90	9.34	2.55	2.88
x = 0.10	1.90	9.87	2.78	2.20
x = 0.15	1.90	9.35	2.65	2.09
x = 0.50	1.90	7.29	2.38	1.36
x = 0.80	1.46	2.26	1.25	1.18
x = 1.00	0.96	2.02	0.24	1.20

The results showed that the R–R interactions remain constant for the samples with $0 \leq x \leq 0.5$ (Table 2). The lower values of exchange interactions obtained for x = 0.8 and x = 1.0 may be related to the presence of foreign magnetic phases in these samples and the superstructure of the last one. As Ni concentration increases, R–T and T–T interactions weaken, but the latter is almost one order of magnitude higher than the others. The negative sign of J_{RT} means the antiparallel coupling between R and T moments. Taking μ_{Gd} = 7 μ_B and μ_{Tb} = 9 μ_B, we determined the average magnetic moment per 3*d* sublattice (2 $\mu_{3d\text{-}MFT}$), as a function of x (Table 2). The obtained values are slightly higher than those derived from M_S (Table 1), but the same decreasing trend is preserved. One has to note that M_s was determined from the magnetization curve up to 7 T, while for MFT analysis, we used

magnetization curves measured at 5 T. Based on the obtained results, we claim that the weakening of R–T and T–T interactions is responsible for decreasing T_C and the magnetic moment of the 3*d* sublattice in the investigated system.

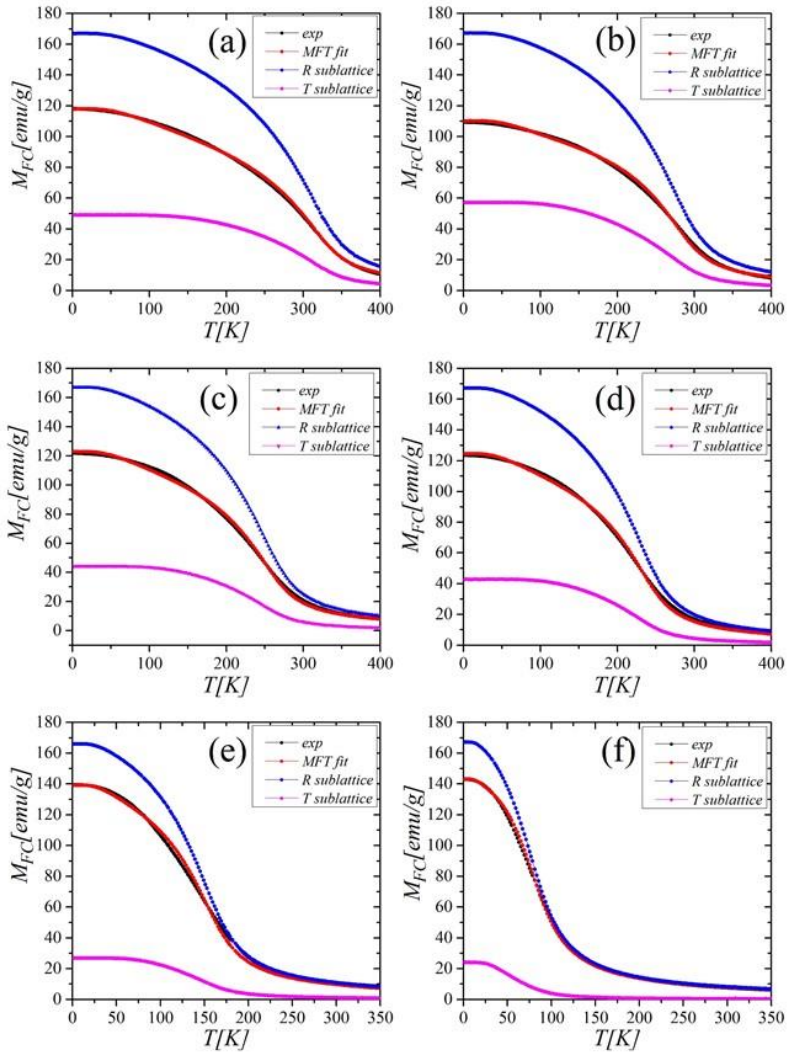

Figure 7. The $M_{FC}(T)$ dependence at $\mu_0 H$ =5 T (*exp*) and the results of MFT analysis for $Gd_{0.4}Tb_{0.6}(Co_{1-x}Ni_x)_2$ compounds with concentrations x = 0.00; 0.05; 0.10; 0.15; 0.50; and 0.80 (figures (**a**–**f**), respectively).

The Arrott plots (not shown here) indicate that the investigated compounds undergo a phase transition of the second-order (SOPT). To confirm the observation, we determined the type of phase transition using the Landau expression for the magnetic free energy (*F*) [14]:

$$F = \frac{1}{2}a(T)M^2 + \frac{1}{4}b(T)M^4 + \frac{1}{6}c(T)M^6 - \mu_0 HM \quad (1)$$

The temperature dependence of Landau coefficients $a(T)$, $b(T)$, and $c(T)$ are usually used to identify the type of phase transition. They are accessible through the following relation between M and H [15]:

$$\mu_0 H = a(T)M + b(T)M^3 + c(T)M^5 \quad (2)$$

Essentially, the order of the magnetic transition is governed by the sign of $b(T)$. The FOPT takes place if $b(T_C) < 0$, while the SOPT occurs when $b(T_C) \geq 0$ in the vicinity of T_C [15]. The coefficients were determined by fitting Equation (2) to magnetic isotherms $\mu_0 H(M)$ (not shown here).

As shown in Figure 8, the $a(T)$ exhibits a minimum nearby T_C. The $b(T)$ parameter is positive, proving that we are dealing with SOPT and confirming the result obtained from Arrott's plots.

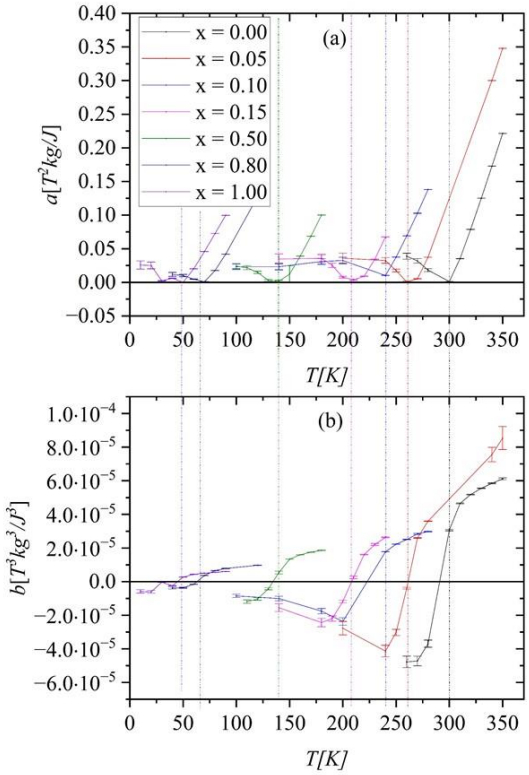

Figure 8. The temperature dependence of Landau coefficients $a(T)$ and $b(T)$—figures (**a**) and (**b**), respectively. Vertical lines indicate transition temperatures (T_C) for alloys with different x.

2.3. Magnetocaloric Properties

In materials showing SOPT, the magnetic entropy change is lower than in those with FOPT. However, the former usually has a broader working temperature range. This property of SOPT is significant for potential applications, e.g., in magnetic refrigerators [16].

To calculate the magnetic entropy change ΔS_M based on the measured magnetic isotherms, we used Maxwell's relation:

$$\Delta S_M(M,H) = \int_{H_0}^{H_1} \left(\frac{\partial M}{\partial T}\right)_H dH, \tag{3}$$

where H_0 and H_1 are the initial and final magnetic fields in the above formula, respectively.

As can be seen in Figure 9, the maxima of the entropy changes $-\Delta S_M$ occur near T_C, which is typical for compounds exhibiting SOPT. It is noteworthy that the value of $|\Delta S_M|^{\max}$ increases with growing nickel content (Figure 9h, Table 3). In addition, we found that the ΔS_M curves are only symmetrical to T_C in a limited temperature range ($T_C \pm 50$ K). For the compound with $x = 0.0$, this effect may be related to a partial reorientation of the Tb spin toward the easy axis direction [6,27]. For $x \neq 0$, this may also be influenced by the magnetic disorder. The height and the width of curves increase with the growth of the magnetic field for all compounds. As a result, the value of δT_{FWHM} (called the operating temperature and defined as the full width at half-maximum of the $-\Delta S_M$ peak) also increases with $\mu_0 H$.

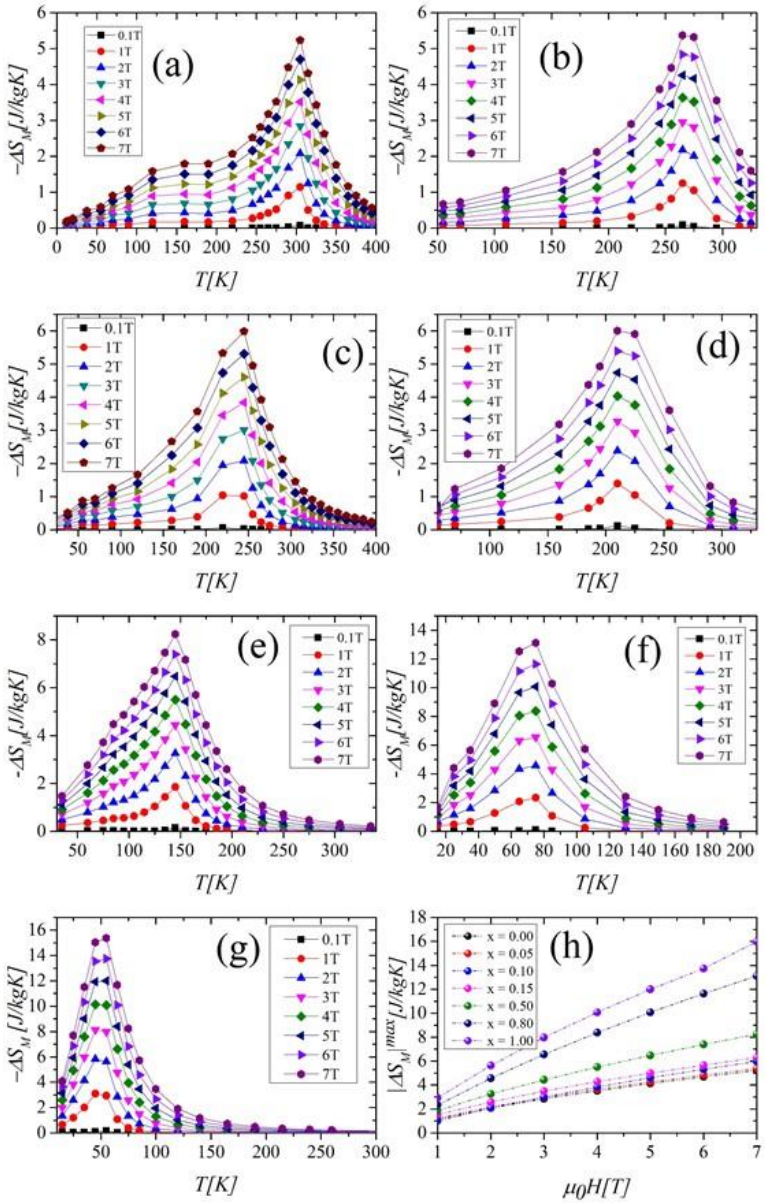

Figure 9. Magnetic entropy changes $-\Delta S_M$ as a function of temperature for samples with x = 0.00 (**a**), 0.05 (**b**), 0.10 (**c**), 0.15 (**d**), 0.50 (**e**), 0.80 (**f**), 1.00 (**g**). Variation of the maximum of the entropy changes $|\Delta S_M|^{\max}$ with the growth of a magnetic field (**h**).

Table 3. The maximum of the entropy changes $|\Delta S_M|^{\max}$, *RC*, *RCP*, and δT_{FWHM} parameters as a function of x in $Gd_{0.4}Tb_{0.6}(Co_{1-x}Ni_x)_2$ compounds. All data are for the magnetic field of 5 T.

$Gd_{0.4}Tb_{0.6}(Co_{1-x}Ni_x)_2$	$\lvert\Delta S_M\rvert^{max}$ [J/kgK]	*RC* [J/kg]	*RCP* [J/kg]	δT_{FWHM} [K]
x = 0.00	4.13	167.23	210.52	50.03
x = 0.05	4.26	190.79	230.06	54.06
x = 0.10	4.60	301.24	381.29	82.89
x = 0.15	5.00	372.01	535.62	114.03
x = 0.50	6.47	406.65	559.69	86.45
x = 0.80	10.07	467.81	623.84	61.96
x = 1.00	11.99	455.58	570.39	47.56

The most significant rise of the δT_{FWHM} values occurs for the compound with $x = 0.15$ (Figure 10a). To assess the cooling efficiency, we calculated the relative cooling power parameter *RCP* using the formula:

$$RCP = |\Delta S_M|^{max} \delta T_{FWHM} \quad (4)$$

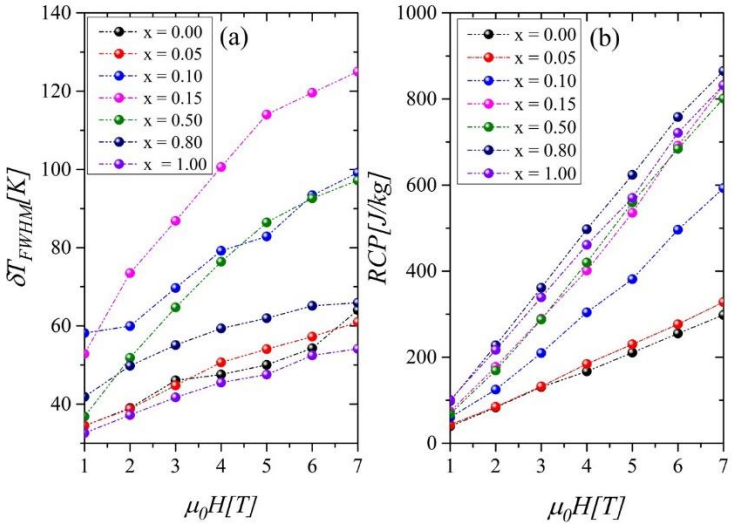

Figure 10. Operating temperatures δT_{FWHM} (**a**) and *RCP* parameters as a function of a magnetic field (**b**).

The cooling efficiency was also evaluated by using the value of refrigerant capacity (*RC*), defined as an amount of the heat that can be transferred from the cold end (at T_{cold}) to the hot end (at T_{hot}):

$$RC = \int_{T_{cold}}^{T_{hot}} |\Delta S_M|^{max} dT. \quad (5)$$

The *RCP* parameters vs. $\mu_0 H$ show the most rapid increase for Ni-rich samples, in which the presence of foreign phases was detected (Figure 10b). The $|\Delta S_M|^{max}$, *RC*, *RCP*, and δT_{FWHM} parameters for all investigated samples are collected in Table 3.

2.4. Electrical Resistivity

The electrical resistivity as a function of temperature for the investigated compounds is presented in Figure 11. We analyzed experimental data using Matthiessen's rule, which combines individual contributions to the resistivity according to [28]:

$$\rho(T) = \rho_0 + \rho_{ph}(T) + \rho_{s-d}(T) + \rho_{e-e}(T). \quad (6)$$

In the formula, ρ_0 indicates residual resistivity, which is temperature independent but strongly depends on the crystal structure [28]. $\rho_{ph}(T)$, $\rho_{s\text{-}d}(T)$ and $\rho_{e\text{-}e}(T)$ are the contributions from electron–phonon scattering, *s*–*d* scattering and electron–electron scattering, respectively [29,30].

Considering the temperature dependence of the individual contributions, Equation (6) for low temperatures takes the form:

$$\rho(T) = \rho_0 + \alpha T^5 - \beta T^3 + \omega T^2 \quad (7)$$

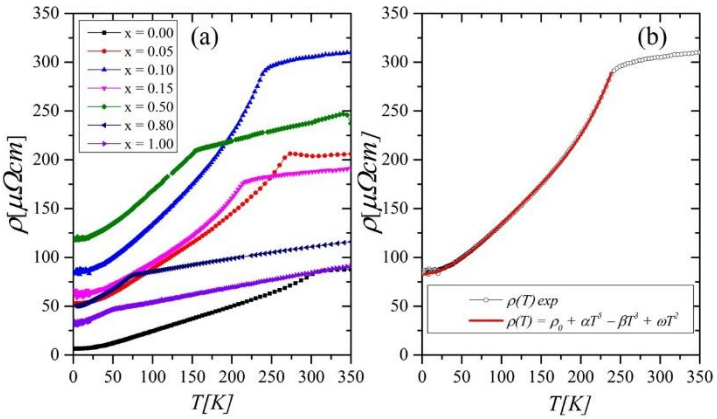

Figure 11. (**a**) Electrical resistivity $\rho(T)$ for the $Gd_{0.4}Tb_{0.6}(Co_{1-x}Ni_x)_2$ compounds, (**b**) the fit of the experimental $\rho(T)$ for $x = 0.10$, according to Formula (7).

All the studied compounds show an evident change in the slope of the $\rho(T)$ curves at the Curie temperatures T_{CR}, which were determined from the $d\rho/dT$ (not presented here). The values of T_{CR} are in reasonable agreement with those obtained from magnetic studies. The experimental data of $\rho(T)$ fitted very well with Formula (7) below T_{CR}, as shown in Figure 11b for the sample with x = 0.10. The resulting parameters α, β, ω, residual resistivity ρ_0, and T_{CR} are collected in Table 4. One can notice that the amplitudes of individual contributions to the resistivity (α, β, ω) show an increasing tendency with the growth of nickel content. The rise of the value of the β parameter, which reflects *s–d* scattering, is due to the substitution of Ni for Co and increasing the number of 3*d* electrons in the band, which may influence the scattering centers of the *d* states. An increasing number of 3*d* electrons can also lead to enhanced electron–electron scattering, which was reflected in the growth of the ω parameter. The behavior of residual resistivity as a function of nickel concentration $\rho_0(x)$ satisfies the Nordheim rule [31]. Namely, the highest value of the ρ_0 is reached for $x = 0.50$ (Figure 3 right axis). Similar behavior is often observed in alloys during doping. The substitution of one type of atom by others generally leads to a disorder of the compound's crystal structure, which manifests as an increase in residual resistivity. It is worth noting that magnetic parameters, such as $H_c(x)$ and $(M_{FC}\text{-}M_{ZFC})$ (x), also showed a similar behavior as $\rho_0(x)$, which indicates that structural disorder may be responsible for the observed trends.

Table 4. The Curie temperatures T_{CR} from resistivity measurements, residual resistivity ρ_0, and fitting parameters from the Equation (7).

$Gd_{0.4}Tb_{0.6}(Co_{1-x}Ni_x)_2$	T_{CR} [K]	ρ_0 [μΩcm]	α	β	ω
x = 0.00	294.4	6.38	$3.70\cdot10^{-11}$	$9.38\cdot10^{-6}$	$2.67\cdot10^{-3}$
x = 0.05	260.6	53.00	$9.41\cdot10^{-11}$	$1.84\cdot10^{-5}$	$5.23\cdot10^{-3}$
x = 0.10	240.1	84.75	$2.26\cdot10^{-10}$	$3.12\cdot10^{-5}$	$8.2\cdot10^{-3}$
x = 0.15	208.2	63.74	$1.45\cdot10^{-10}$	$1.72\cdot10^{-5}$	$4.74\cdot10^{-3}$
x = 0.50	141.0	118.47	$1.81\cdot10^{-10}$	$3.07\cdot10^{-5}$	$7.86\cdot10^{-3}$
x = 0.80	66.0	50.41	$6.20\cdot10^{-9}$	$1.24\cdot10^{-4}$	$1.25\cdot10^{-2}$
x = 1.00	54.2	34.62	$1.40\cdot10^{-9}$	$1.09\cdot10^{-4}$	$1.07\cdot10^{-2}$

2.5. X-ray Photoelectron Spectroscopy (XPS)

Figure 12 presents the XPS valence band spectra of the $Gd_{0.4}Tb_{0.6}(Co_{1-x}Ni_x)_2$ compounds in the binding energy range from −15 eV to 2 eV. In the case of pure rare earth elements, the Gd4*f* states are visible at −8 eV, while the Tb4*f* ones form the multiplet consisting of several lines located at −10.2 eV, −9.1 eV,−7.4 eV, −2 eV [32]. In the compounds under investigation, the first three Tb4*f* contributions and the Gd4*f* one overlap to form a wide band, not dependent on the Ni concentration. Bands near the Fermi level (E_F) are

dominated by Co3*d* and *Ni*3*d* states that form one shared 3*d* band, and they overshade the ${}^8S_{7/2}$ contributions of Tb occurring at −2 eV.

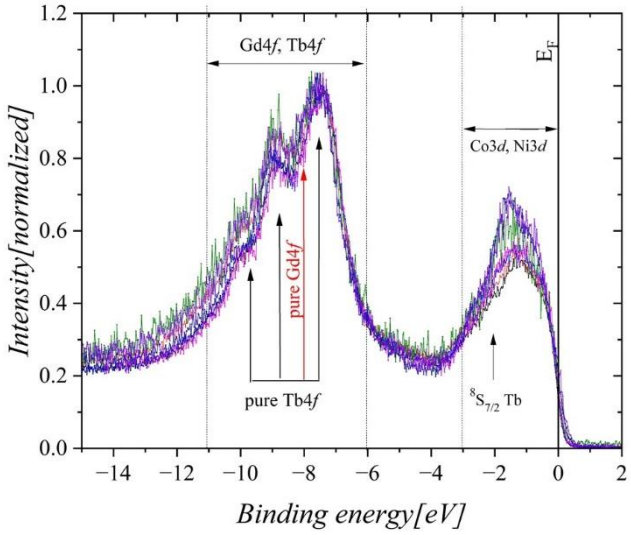

Figure 12. The XPS valence band of $Gd_{0.4}Tb_{0.6}(Co_{1x}Ni_x)_2$. The spectra were normalized to the maximum intensity in this energy range. Vertical arrows show the positions of all spectral lines observed in elemental Gd, Tb, Co, and Ni.

An evident change in the shape of the 3*d* valence band is observed when nickel content increases (Figure 13). In the energy range from 0 eV to −3 eV, the band intensity increases with growing Ni content. Slightly less increment is visible at the Fermi level (inset (b) in Figure 13). Simultaneously, a shift in the maximum intensity of the 3*d* states toward higher binding energies is observed (inset (a) in Figure 13).

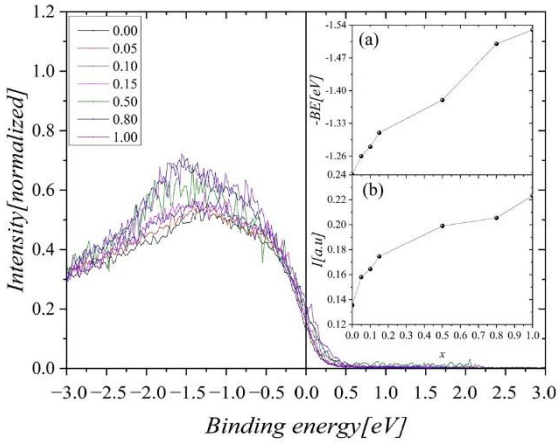

Figure 13. The XPS valence band of $Gd_{0.4}Tb_{0.6}(Co_{1x}Ni_x)_2$ near the Fermi level. Inset (**a**) shows the position of the maximum of 3*d* states contribution and inset (**b**) presents the intensity at the Fermi level, both as a function of Ni concentration.

From the multiplet splitting of the Co3*s* (Figure 14), we obtained information about the magnetic moments μ_{Co}. The multiplet splitting of the 3*s* spectra of 3*d* metals occurs due to the exchange interaction between unfilled 3*d* and 3*s* (ionized) shells [33]. As a result, two final states are observed, and the equation gives the intensity relation of these two peaks [34]:

$$\frac{I_1}{I_2} = \frac{S+1}{S} \quad (8)$$

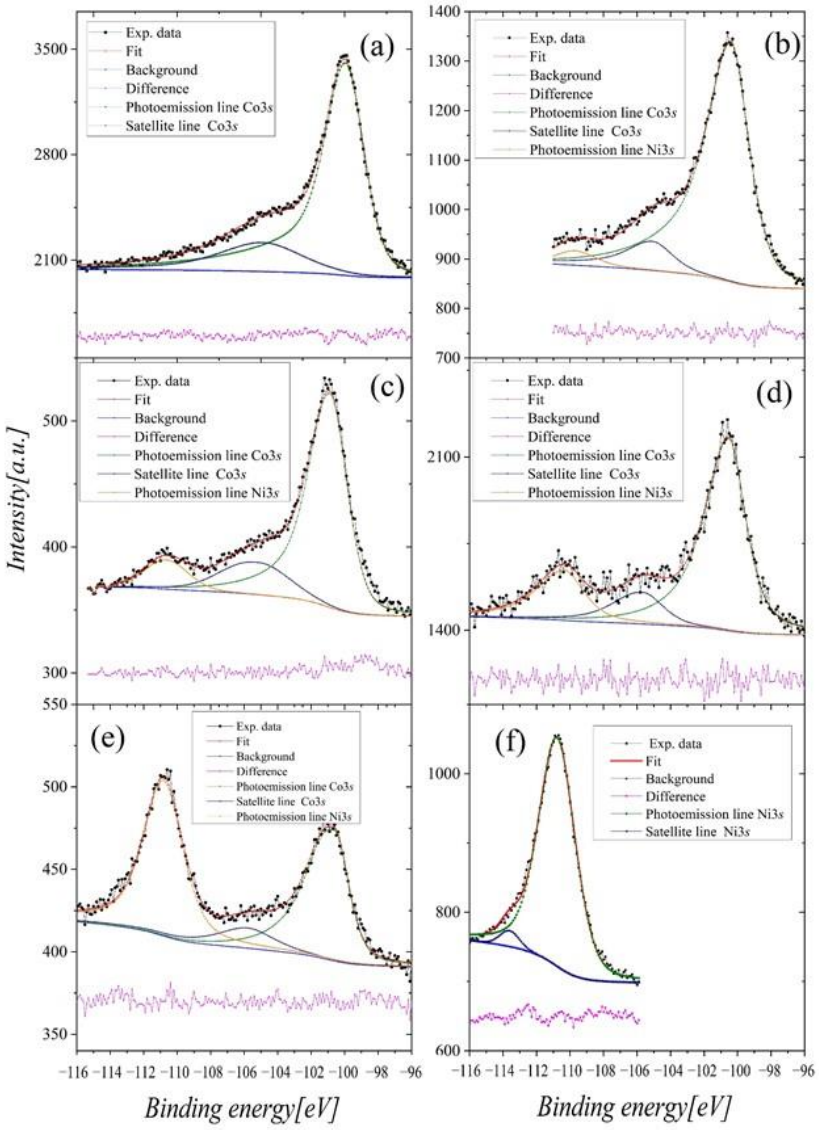

Figure 14. The splitting of the Co3*s* and Ni3*s* lines in $Gd_{0.4}Tb_{0.6}(Co_{1x}Ni_x)_2$. The plots (**a**)–(**f**) concern samples with concentrations x = 0.0, 0.05, 0.10, 0.15, 0.50 and 1.0, respectively.

Here, S is the spin of the unpaired 3*d* electrons, I_1 and I_2 are intensities of the main and the satellite 3*s* line, respectively. The magnetic moment of the Co can be estimated using Formula [35]:

$$\mu_{Co} = 2\mu_B\sqrt{S(S+1)} \quad (9)$$

The μ_{Ni} was similarly estimated only for x = 1, since the Ni 3*s* satellite lines are hardly resolved in XPS spectra for lower Ni concentration.

The I_1/I_2 ratio (Equation (8)) was evaluated by fitting the Co3*s* and Ni3*s* lines applying iterative Shirley background and using the combination of Gaussian–Lorentz curves. This procedure enabled us to reproduce the main shape line and obtain the intensity of the individual contributions [36] (Figure 14). Using the above-described approach, we got the following values of the μ_{Co}: 0.95 μ_B, 0.80 μ_B, 1.02 μ_B, 0.97 μ_B and 0.98 μ_B for x = 0.0, 0.05, 0.10, 0.15 and 0.50, respectively. The values of μ_{Co} deviate slightly from those obtained from the saturation magnetization and the MFT calculations. However, we must remember that the XPS experiment was performed in different conditions than the previous ones (room temperature, no magnetic field). Furthermore, since the intensity of the Co3s line became weaker with increasing nickel content, the resulting moments were subjected to greater error. The magnetic moment of Ni estimated from the fit presented in Figure 14f

was equal to 0.05 μ_B. It is worth noting that the result confirms the rightness of our earlier assumption about the small magnetic moment on nickel.

2.6. Ab Initio Results

Quantitative magnetic results of ab initio calculations (M_S and μ_{3d}) are shown in Table 1. The magnetization M_S for compositions $Gd_{0.375}Tb_{0.625}(Co_{1-x}Ni_x)_2$ was estimated using the relation: $M_S = 0.375 \cdot \overline{\mu}_{Gd} + 0.625 \cdot \overline{\mu}_{Tb} + 2 \cdot ((1-x) \cdot \overline{\mu}_{Co} + x \cdot \overline{\mu}_{Ni})$, where the z-projected average R4f magnetic moment was evaluated using the formula $\mu_R^{4f} = g_J \cdot (L+S)$ [35]. The values of μ_{Co} and μ_{Ni} were taken from ab initio calculations. Since within the superstructures, $Gd_3Tb_5Co_{16-n}Ni_n$ (n = 0, 2, 4, 6, 8, 16) applied in calculations, each component atom occupies several Wyckoff positions with specified multiplicity, and the $\overline{\mu}_{Co}$, $\overline{\mu}_{Ni}$ were obtained by averaging local (Co and Ni) atomic moments over Wyckoff positions. Due to the lack of ab initio results for the orbital angular momentum of R, we assumed L = 3, S = 3, and L = 0, S = 7/2, corresponding to Tb and Gd in an ionic state with valency 3^+ [35].

The calculated T and R local magnetic moments align oppositely in agreement with experimental observations. Furthermore, the dependence of calculated magnetization M_S on Ni content quantitatively follows the determined experiment. Detailed analysis displayed that with increasing Ni content in the range x = 0.0–0.5, the magnitudes of both $\overline{\mu}_{Co}$ and $\overline{\mu}_{Ni}$ decrease in the range of 1.28–1.21μ_B and 0.25–0.21μ_B, respectively. Only in the Ni-rich $Gd_{0.375}Tb_{0.625}Ni_2$ compound the average $\overline{\mu}_{Ni}$ has dropped to 0.13 μ_B. For the considered Ni concentrations, the magnetization M_S increases following the simple magnetic dilution in the Co-Ni sublattice, where the higher magnetic moment of Co is replaced by the lower one of Ni. The linear fit to calculated M_S yields the relation $M_S(x)$ = 2.104 x + 5.942(R^2 = 0.998). The values of M_S estimated with the formula are compared with the experimental ones in Table 1. Some discrepancy between experimental data and theoretical estimates occurs for x = 0.1 and x = 0.15, where calculations underestimate M_S but at most by a few percent. It can be related to the atomic disorder, as evidenced by the residual resistivity measurements (see Figure 3). The more significant deviations occur between the calculated average μ_{3d} and derived from the MFT approach (Table 1). Although both results show diminishing 3d lattice magnetization, the ab initio calculations give the μ_{3d} moment systematically overestimated.

To get insight into the microscopic origin of the changes of XPS spectra with increasing Ni content in the $Gd_{0.4}Tb_{0.6}(Co_{1-x}Ni_x)_2$ series, we performed a detailed analysis of the electronic densities of states (DOS) obtained from ab initio calculations. Figure 15 confirms an almost strict correspondence between the shape of the XPS spectrum and the calculated DOS in $Gd_{0.4}Tb_{0.6}(Co_{0.5}Ni_{0.5})_2$. Noticeable inconsistencies between the DOS and the XPS spectrum exist near the Fermi level and in the range of the R4f band. We presented the explanation of the discrepancies in [6].

In the observed XPS spectra related to the 3d band (Figure 13a), the intensity increases and the maximum shifts simultaneously to higher BE energy with rising Ni content. To understand the reasons for such behavior in the first stage, we analyze the DOS of endpoint compounds presented in Figure 16.

The valence band structure of the endpoint compounds comprises the 4f states of R atoms, lying deeply (around −8 eV) below Fermi energy (ε_F) and the 3d states of Co (Ni), forming the band at the energy range −4–2 eV split into bonding and antibonding subbands. The minority spin 3d bands (down arrow) in both compounds are almost entirely occupied. Upon the Co/Ni substitution, the band only narrows slightly and shifts minutely toward the Fermi level.

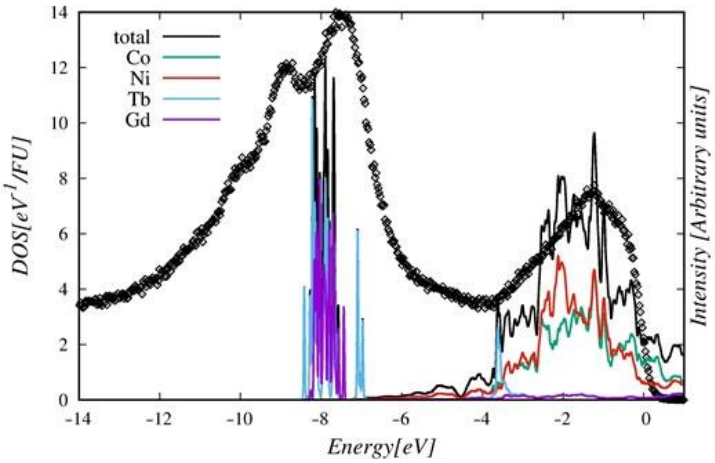

Figure 15. Atomic resolved and total DOS in $Gd_{0.4}Tb_{0.6}(Co_{0.5}Ni_{0.5})_2$ (solid lines), compared with the scaled XPS spectra (black points).

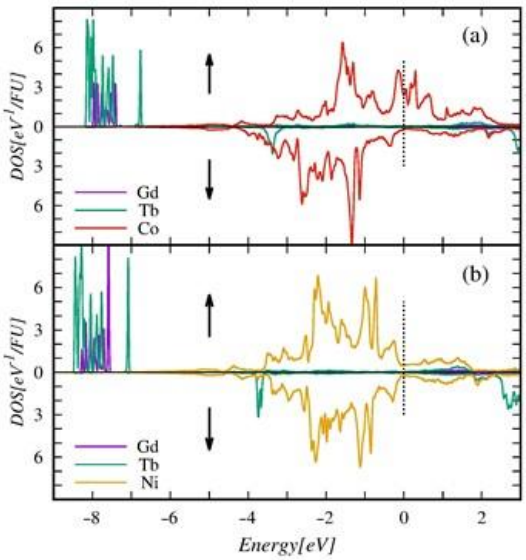

Figure 16. Spin resolved atomic contributions to the total density of states (DOS) calculated for end compounds: $Gd_{0.375}Tb_{0.625}Co_2$—(**a**) and $Gd_{0.375}Tb_{0.625}Ni_2$—(**b**). The energy scale zero is shifted to the Fermi level ε_F (vertical dot lines). The arrows distinguish the spin orientations of electronic states.

Additional 3*d* electrons contributed by Ni atoms populate only the majority spin 3*d* bands. The partially populated antibonding majority spin states in the $Gd_{0.375}Tb_{0.625}Co_2$ get fully occupied in the $Gd_{0.375}Tb_{0.625}Ni_2$. In effect, the majority spin 3*d* band in the second compound shifts toward higher binding energies and becomes slightly narrower. It is worth noting that the bands of 3*d* states with opposite spin directions in $Gd_{0.375}Tb_{0.625}(Co_{0.5}Ni_{0.5})_2$ are almost symmetrical, which explains the vanishingly small magnitude of $\overline{\mu}_{Ni}$ appearing in the compound.

The variation of the calculated band structure upon Co/Ni substitution in the $Gd_{0.4}Tb_{0.6}(Co_{1-x}Ni_x)_2$ series is displayed in Figure 17a. As concern the minority spin 3*d* band, besides a slight shift toward the Fermi level, the changes are negligible. The apparent changes occur in the majority spin bands DOS, in which the dominant peak shifts toward higher binding energy by almost 0.5 eV. The magnitude of the shift is close to that displayed by experimental spectra (Figure 13a). Figure 17b shows the variation of separated contributions of constituent Co and Ni atoms to the 3*d* band upon increasing Ni concentration. As expected, the amplitude of co-contribution decreases while that of Ni increases with the growing Ni content. However, detailed inspection indicates that

upon Co/Ni substitution, the Co3*d* states shift minutely toward the Fermi level when the dominant peak of the Ni contribution shifts noticeably in the opposite direction. The last effect could explain the observed shift of maximum intensity of the XPS spectra, related to the 3*d* band, with rising concentration of Ni in $Gd_{0.4}Tb_{0.6}(Co_{1-x}Ni_x)_2$ series.

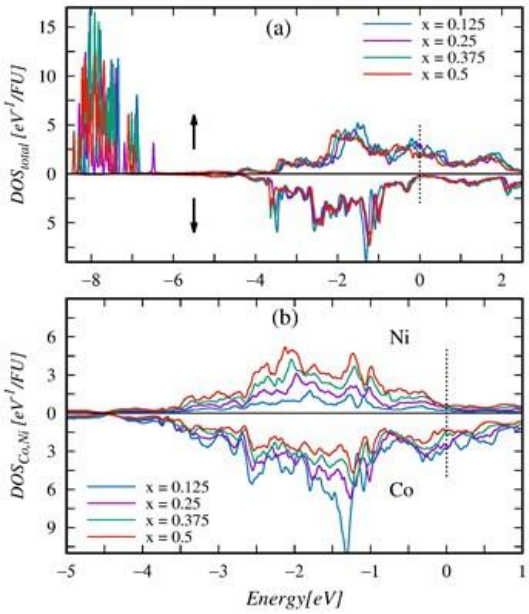

Figure 17. Spin resolved the total density of states DOS_{total} (**a**), and Ni and Co contributions to the DOS (**b**) in the $Gd_{0.4}Tb_{0.6}(Co_{1-x}Ni_x)_2$ series. For a detailed description, see the caption of Figure 16.

3. Methods and Materials

The $Gd_{0.4}Tb_{0.6}(Co_{1-x}Ni_x)_2$ samples x = 0.00, 0.05, 0.10, 0.15, 0.50, 0.80, 1.00 were prepared by arc melting method from high purity elements (99.99% purity) under argon atmosphere. An excess of 1% wt. of gadolinium and terbium was added to overcome weight losses during the melting. The samples have been re-melted several times to obtain the homogeneity of prepared compounds. Afterward, the as-cast samples were wrapped in tantalum foil, placed in a quartz tube, and annealed at 800 °C for two weeks. The crystal structure was determined by the X-ray diffraction technique using the XRD diffractometer Empyrean (PANalytical, Malvern, UK). The measurements were performed at room temperature with Cu K_α source and 2θ changing from 15 to 140 degrees. All magnetic measurements were carried out using the SQUID magnetometer MPMS XL–7 (Quantum Design, San Diego, CA, USA) in the temperature range from 2 K to 350 K–400 K under a magnetic field up to 7 T. The electronic structure of the investigated compounds was studied using the XPS method. The XPS spectra were obtained with monochromatized Al K_α radiation ($h\omega$ = 1486.6 eV) at room temperature using PHI 5700/660 physical electronics spectrometer. All spectra were measured immediately after breaking the sample in a 10^{-9} Torr vacuum. The breaking in the high vacuum resulted in clean surfaces free of oxygen and carbon contamination. Electrical resistivity was carried out by the PPMS system. The samples were cut into rectangular shapes with dimensions of 1 × 1 × 3 mm. The measurements were performed in the temperature range of 2 K–350 K.

The ab initio electronic structure calculations for selected concentrations of $Gd_{0.4}Tb_{0.6}(Co_{1-x}Ni_x)_2$ were performed using the FP-LAPW method [37] implemented in the WIEN2k computer programs [38]. In the present investigations, we applied the same approach and computational setup used in calculations for the reference $Gd_{0.4}Tb_{0.6}Co_2$ compound [6].

We followed the supercell approach to simulate the fractional concentration of Co-Ni elements in $Gd_{0.4}Tb_{0.6}(Co_{1-x}Ni_x)_2$ alloys. We adopted the superstructure $Gd_3Tb_5Co_{16}$ applied in [6] in the present calculations as a base supercell. The concentrations x_{Ni} =

0.125, 0.25, 0.375, and 0.50 were simulated using superstructures $Gd_3Tb_5Co_{16-n}Ni_n$ where, respectively, 2, 4, 6, 8 Co atoms were replaced by Ni ones at selected sites. We are aware that for each considered concentration, there is an enormous number of Co-Ni configurations. However, we assumed that a single reasonably selected configuration (not of cluster shape) can reproduce essential features of the electronic structure of $Gd_{0.4}Tb_{0.6}(Co_{1-x}Ni_x)_2$ alloys.

4. Conclusions

The new class of the $Gd_{0.4}Tb_{0.6}(Co_{1-x}Ni_x)_2$ intermetallic compounds with the Laves phase structure of C15 type was synthesized. Structural, electronic, and magnetic properties were studied using experimental and theoretical methods.

The experimental and theoretical studies (ab initio and MFT) have shown that the magnetic moments of the R and 3*d* subnets align oppositely. With increasing nickel content, the values of 2 μ_{3d} decreased. Values of Curie temperatures determined by different methods were consistent and diminished with growing nickel content too. Arrott plots and Landau's coefficients indicated a second-order phase transition in all studied compounds.

The values of the maximum entropy change $|\Delta S_M|^{max}$, obtained under the magnetic field change of 5 T, increased with growing Ni content from 4.13 [J/kgK] to 11.99 [J/kgK] for samples with x = 0.0 and 1.0, respectively. *RCP* parameters also grew significantly with Ni concentration.

Presented results revealed that the replacement of Co with Ni enhanced the magnetocaloric effect in the $Gd_{0.4}Tb_{0.6}(Co_{1-x}Ni_x)_2$, making these materials more attractive in terms of potential applications in magnetic refrigeration. An additional advantage is that they have minimal losses observed in hysteresis loops.

Our studies have also shown that the substitution of Ni in place of Co significantly affects the resistive properties of investigated compounds. Due to a disorder of the compound's crystal structure, an increase in the residual resistivity increases up to x = 0.50, which follows Nordheim's rule. A similar variation of $H_c(x)$ and $(M_{FC}\text{-}M_{ZFC})(x)$ indicates that structural disorder may be responsible for magnetic properties.

Both XPS measurements and ab initio calculations revealed that Co3*d* and Ni3*d* states dominate the shape of the valence band near the Fermi level. With growing Ni contents, the observed intensity of the XPS spectra corresponding to 3*d* bands increases, and its maximum shifts to the higher binding energy. Ni doping, however, did not affect the positions and shapes of the Gd4*f* and Tb4*f* lines. Ab initio calculations confirmed the XPS picture.

Author Contributions: Conceptualization, G.C. and M.S.; methodology, M.S., A.C., A.B. and G.Z.; theoretical calculations, J.D.; formal analysis, A.C. and G.Z.; validation, G.C. and J.D.; writing—original draft preparation, G.C., J.D. and M.S. All authors have read and agreed to the published version of the manuscript.

Funding: This research received no external funding.

Institutional Review Board Statement: Not applicable.

Conflicts of Interest: The authors declare no conflict of interest.

References

1. Gratz, E.; Markosyan, A.S. Physical properties of RCo_2 Laves phases. *J. Phys. Condens. Matter* **2001**, *13*, R385–R413. [CrossRef]
2. Baranov, N.; Yermakov, A.A.; Pirogov, A.N.; Proshkin, A.; Gvasaliya, S.N.; Podlesnyak, A.A. Irreversibility of the magnetic state of $Tm_{1-x}Tb_xCo_2$ revealed by specific heat, electrical resistivity, and neutron diffraction measurements. *Phys. Rev. B* **2006**, *73*, 104445. [CrossRef]
3. Duc, N.H.; Goto, T. Itinerant electron metamagnetism of Co-sublattice in the lanthanide-cobalt intermetallics. In *Handbook on the Physics and Chemistry of RareEarths*; Gschneidner, K.A., Jr., Eyring, L., Eds.; North-Holland: Amsterdam, The Netherlands, 1999; Volume 26, pp. 177–264.
4. Goto, T.; Fukamichi, K.; Sakakibara, T.; Komatsu, H. Itinerant electron metamagnetism in YCo_2. *Solid State Commun.* **1989**, *72*, 945–947. [CrossRef]

5. Goto, T.; Sakakibara, T.; Murata, K.; Komatsu, H.; Fukamichi, K. Itinerant electron metamagnetism in YCo_2 and $LuCo_2$. *J. Magn. Magn. Mater.* **1990**, *90*, 700–702. [CrossRef]
6. Sikora, M.; Bajorek, A.; Chrobak, A.; Deniszczyk, J.; Ziółkowski, G.; Chełkowska, G. Magnetic properties and electronic structure of the $Gd_{0.4}Tb_{0.6}Co_2$ compound. *Materials* **2020**, *13*, 5481. [CrossRef] [PubMed]
7. Zhou, K.W.; Zhuang, Y.H.; Li, J.Q.; Deng, J.Q.; Zhu, Q.M. Magnetocaloric effect in $(Gd_{1-x}Tb_x)Co_2$. *Solid State Commun.* **2006**, *137*, 275–277. [CrossRef]
8. Saville, A.I.; Creuziger, A.; Mitchell, E.B.; Vogel, S.C.; Benzing, J.T.; Klemm-Toole, J.; Clarke, K.D.; Clarke, A.J. MAUD Rietveld Refinement Software for Neutron Diffraction Texture Studies of Single-and Dual-Phase Materials. *Integr. Mater. Manuf. Innov.* **2021**, *10*, 461–487. [CrossRef]
9. Lutterotti, L. MAUD Tutorial—Instrumentation Broadening Determination. Available online: https://www.researchgate.net/publication/228868859 (accessed on 20 September 2022).
10. Lingwei, L.; Nishimura, K.; Tamei, D.; Mori, K. Structure, transport properties and magnetocaloric effect in $Gd(Co_{1-x}Ni_x)_2$ pseudobinary compounds. *Solid State Commun.* **2008**, *145*, 427–431.
11. Kaneko, T.; Marumo, K.; Miura, S.; Kido, G.; Abe, S.; Yoshida, H.; Kamigaki, K.; Nakagawa, Y. High-field susceptibility of pseudobinary compounds $Gd(Co_{1-x}Ni_x)_2$. *Phys. B* **1988**, *149*, 334–339. [CrossRef]
12. Miiller, W.; Causeret, L.; Ling, C.D. Frustrated magnetism and local structural disorder in pyrochlore-type $Bi_{1.89}Fe_{1.16}Nb_{0.95}O_{6.95}$. *J. Phys. Condens. Matter* **2010**, *22*, 486004. [CrossRef]
13. Dubowik, J.; Gościańska, I.; Kudryavtsev, Y.V.; Oksenenko, V.A. Structure and magnetism of Co_2CrAl Heusler alloy films. *Mater. Sci.* **2007**, *25*, 1281–1287.
14. Duc, N.H.; Hien, T.D.; Mai, P.P.; Ngan, N.H.K.; Sinh, N.H.; Brommer, P.E.; Franse, J.J.M. The magnetic phase transitions in (Tb,Ho)Co_2, and (Tb, Y)Co_2, compounds. *Phys. B Condens. Matter* **1989**, *160*, 199–203. [CrossRef]
15. Ćwik, J. Magnetism and magnetocaloric effect in multicomponent Laves phase compounds: Study and comparative analysis. *J. Solid State Chem.* **2014**, *209*, 13–22. [CrossRef]
16. Tishin, A.M. Magnetocaloric effect: Current situation and future trends. *J. Magn. Magn. Mater.* **2007**, *316*, 351–357. [CrossRef]
17. Wang, J.L.; Tang, C.C.; Wu, G.H.; Liu, Q.L.; Tang, N.; Wang, W.Q.; Wang, W.H.; Yang, F.M.; Liang, J.K.; de Boer, F.R.; et al. Structure and magneto-history behavior of $DyNi_2Mn$. *Solid State Commun.* **2002**, *121*, 615–618. [CrossRef]
18. Singh, J.K.; Sureh, K.G.; Rana, D.S.; Nigam, A.K.; Malik, S. Role of Fe substitution on the anomalous magnetocaloric and magnetoresistance behaviour in $Tb(Ni_{1-x}Fe_x)_2$ compounds. *J. Phys. Condens. Matter* **2006**, *18*, 10775–10786. [CrossRef]
19. Balli, M.; Fruchart, D.; Gignoux, D. Effect of Ni substitution on the magnetic and magnetocaloric properties of the $Dy(Co_{1-x}Ni_x)_2$ Laves phase. *J. Phys. D Appl. Phys.* **2007**, *40*, 7601–7605. [CrossRef]
20. Ouyang, Z.W.; Rao, G.H.; Yang, H.F.; Liu, W.F.; Liu, G.Y.; Feng, X.M.; Liang, J.K. Structure and magnetic phase transition in R$(Co_{1-x}Ga_x)_2$ (R = Nd, Gd, Tb, Dy) compounds. *Phys. B* **2004**, *344*, 436–442. [CrossRef]
21. Mizumaki, M.; Yano, K.; Umehara, I.; Ishikawa, F.; Sato, K.; Koizumi, A.; Sakai, N.; Muro, T. Verification of Ni magnetic moment in $GdNi_2$ Laves phase by magnetic circular dichroism measurement. *Phys. Rev. B* **2003**, *67*, 132404. [CrossRef]
22. Fullerton, E.E.; Jiang, J.S.; Bader, S.D. Hard/soft magnetic heterostructures: Model exchange-spring magnets. *J. Magn. Magn. Mater.* **1999**, *200*, 392–404. [CrossRef]
23. Kneller, E.F.; Hawig, R. The exchange-spring magnet: A new material principle for permanent magnets. *IEEE Trans. Magn.* **1991**, *27*, 3560–3588. [CrossRef]
24. Chrobak, A.; Bajorek, A.; Chełkowska, G. Effect of Tb/Gd Substitution on Crystal Structure and Exchange Interactions of $Gd_{1-x}Tb_xNi_3$ Intermetallic Compounds. *Acta Phys. Pol. A* **2012**, *121*, 1132–1135. [CrossRef]
25. Duc, N.H. An evaluation of the R–T spin coupling parameter in the rare earth–transition metal intermetallics. *Phys. Stat. Sol.* **1991**, *164*, 545–552. [CrossRef]
26. Duc, N.H.; Hien, T.D.; Givord, D.; Franse, J.J.M.; de Boer, F.R. Exchange interaction in rare earth- transition metal compounds. *J. Magn. Magn. Matter* **1993**, *124*, 305–311. [CrossRef]
27. Gratz, E.; Goremychkin, E.; Latroche, M.; Hilscher, G.; Rotter, M.; Müller, H.; Lindbaum, A.; Michor, H.; Paul-Boncour, V.; Fernandez-Diaz, T. New magnetic phenomena in $TbNi_2$. *J. Phys. Condens. Matter* **1999**, *11*, 7893–7905. [CrossRef]
28. Meaden, G.T. *Electrical Resistance of Metals*; Springer: New York, NY, USA, 1965. [CrossRef]
29. Steiner, W.; Gratz, E.; Ortbauer, H.; Camen, H.W. Magnetic properties, electrical resistivity and thermal expansion of (Ho,Y)Co_2. *J. Phys. F Metal Phys.* **1978**, *8*, 1525–1537. [CrossRef]
30. Fisk, Z.; Webb, G.W. Electrical Resistivity of Metals. In *Electronic Structure and Properties*; Fradin, F.Y., Ed.; Academic Press, Inc.: New York, NY, USA, 1981; pp. 297–349.
31. Hall, G.L. Nordheim's Theory of the Resistivity of Alloys. *Phys. Rev.* **1959**, *116*, 604–605. [CrossRef]
32. Lang, J.K.; Baer, Y.; Cox, P.A. Study of 4f state and valence band density of state in rare earth metals: II. Experiment and results. *J. Phys. F. Met. Phys.* **1981**, *11*, 121–138. [CrossRef]
33. Hüfner, S. Core levels and final states. In *Photoelectron Spectroscopy*, 3rd ed.; Springer: Berlin/Heidelberg, Germany, 2003.
34. Shabanova, I.N.; Keller, N.V. X-ray photoelectron studies of spine-state changes in 3d metal systems. *Surf. Interface Anal.* **2001**, *32*, 114–116. [CrossRef]
35. Coey, J.M.D. Magnetism of localized electrons on the atom. In *Magnetism and Magnetic Materials*; Cambridge University Press: Cambridge, UK, 2010.

36. *Multipack Software*, Version 9.8.0.19; Ulvac phi, Incorporated: Chigasaki, Japan, 2017.
37. Singh, D.J.; Nordstrom, L. *Plane Waves, Pseudopotentials, and the LAPW Method*, 2nd ed.; Springer Science: New York, NY, USA, 2006; ISBN 978-0-387-28780-5.
38. Blaha, P.; Schwarz, K.; Madsen, G.K.H.; Kvasnicka, D.; Luitz, J.; Laskowski, R.; Tran, F.; Marks, L.D. *WIEN2k, An Augmented Plane Wave + Local Orbitals Program for Calculating Crystal Properties*; Schwarz, K., Ed.; Techn. Universität Wien: Vienna, Austria, 2018; ISBN 3-9501031-1-2.